Journal of Materials Chemistry C

ROYAL SOCIETY OF CHEMISTRY

PAPER

View Article Online
View Journal

Cite this: DOI: 10.1039/d6tc00560h

Molten salt–assisted screen printing of highly textured Zn_2SiO_4 films with enhanced deep UV emission

Jallouli Necib, *[a] Eduard Feldbach,[b] Ivo Romet, [b] Vitali Nagirnyi, [b] Irina Hussainova, [a] Thomas Jüstel [c] and Rocío E. Rojas-Hernandez [ad]

A novel and scalable approach for the fabrication of deep ultraviolet (UV) emitting materials is presented through the synthesis of highly textured zinc silicate films using screen printing assisted by a NaCl–KCl eutectic flux. This work provides the first demonstration of intrinsic deep UV emission in screen-printed Zn_2SiO_4 films and establishes a correlation between processing conditions, interfacial phase evolution, and optical response. The films exhibited strong preferential orientation along the (300) plane with Lotgering factors reaching up to 0.94. Interface analysis reveals the pivotal role of flux-mediated phase transformations in governing film growth dynamics and surface morphology. Detailed luminescence studies identified intense deep UV emission at 4.43 eV (280 nm), attributed to intrinsic electronic transitions within the Zn_2SiO_4 material. Synchrotron radiation studies indicate that the emission involves band-to-band transitions and excitonic processes influenced by the local structural environment. Notably, emission intensity correlates strongly with both crystallographic texturing and the quality of the film–substrate interface, highlighting the key role of interface and structural control in enhancing deep UV emission. The demonstrated method offers a promising pathway for the development of mercury-free and rare-earth-free deep UV emitters for next-generation photonic and optoelectronic applications.

Received 22nd February 2026,
Accepted 9th April 2026

DOI: 10.1039/d6tc00560h

rsc.li/materials-c

1. Introduction

The demand for deep ultraviolet (UV) emitters, particularly in the UV-C (100–280 nm) and UV-B (280–315 nm) spectral ranges, has surged in recent years owing to their critical applications in disinfection, medicine, and agriculture.[1–9] Recent epidemics have further underscored the importance of UV-C radiation for pathogen inactivation,[1,2] highlighting the urgent need for efficient and sustainable deep UV light sources. However, the conventional deep UV emitters such as mercury lamps pose significant environmental and health risks, leading to global initiatives such as the Minamata convention on mercury to phase out their use.[10] Although rare-earth-doped phosphors have been explored as alternatives, their dependence on rare-earth elements presents challenges related to resource availability, cost, and geopolitical constraints.[11,12]

In parallel, deep UV emission has been extensively developed in wide band gap semiconductor systems, particularly AlN and AlGaN alloys, which represent the leading solid-state platform for deep UV light sources.[13–15] However, only a limited number of materials are known to exhibit efficient deep UV emission,[16,17] indicating a restricted materials space in this spectral range. Recent high-throughput computational studies further support this observation by identifying only a small group of rare-earth-free wide band gap compounds with suitable electronic structures for deep UV emission, such as $BeGeN_2$, Mg_3NF_3, and $KCaBr_3$.[17]

Within this framework, selected oxide materials have emerged as promising candidates for deep UV emission, where luminescence arises from intrinsic electronic transitions that are strongly influenced by local structural and defect environments, making precise control over crystallization and defect formation essential for optimizing emission efficiency.[18,19] This structure-sensitive behaviour is exemplified by $ZnAl_2O_4$, where deep UV emission has been linked to excitons perturbed by oxygen vacancies.[20,21] Other wide band gap oxides, including $ZnGa_2O_4$ and $K_2ZrSi_2O_7$, have also demonstrated intrinsic deep UV emission,[22,23] illustrating the capability of these materials to function as rare earth free emitters. Among these materials, zinc silicate (Zn_2SiO_4), with a band gap width ranging from

[a] Department of Mechanical and Industrial Engineering, Tallinn University of Technology, Ehitajate 5, 19180 Tallinn, Estonia. E-mail: Jallouli.necib@taltech.ee
[b] Institute of Physics, University of Tartu, W. Ostwald Str 1, 50411 Tartu, Estonia
[c] FH Münster University of Applied Sciences, Department of Chemical Engineering, Stegerwaldstr. 39, D-48565 Steinfurt, Germany
[d] Electroceramic Department, Instituto de Cerámica y Vidrio, CSIC, Kelsen 5, 28049 Madrid, Spain

5.5 to 6.26 eV according to different studies,[24–27] has gained attention because of its potential for intrinsic deep UV luminescence. While most studies have been focused on doped Zn_2SiO_4 for visible emission, its undoped form remains largely unexplored for UV applications. In our previous investigations, undoped Zn_2SiO_4 powders synthesized *via* sol–gel and molten salt routes exhibited intrinsic UV-B emission,[28,29] demonstrating the potential of Zn_2SiO_4 as a rare-earth-free deep UV emitter. However, the extension of this intrinsic emission behaviour to film form remains limited. The prior studies have been primarily focused on nanocables, nanotubes, or sputtered films.[30–33] For example, Furukawa *et al.*[33] reported a 300 nm emission band in Zn_2SiO_4 thin films synthesized *via* radio frequency magnetron sputtering, whereas Peng *et al.*[34] observed no detectable photoluminescence under similar conditions, illustrating the challenges in achieving consistent deep UV emission. These contrasting results clearly indicate a need for research aimed at understanding how processing conditions, phase evolution, and interfacial reactions govern intrinsic luminescence in Zn_2SiO_4 films. Moreover, the complexity, high energy demand, and cost of sputtering techniques further limit their practical application.

In contrast, solution-based techniques such as screen printing offer a simple, scalable, cost-effective, and environmentally friendly alternative.[35–37] Unlike vacuum-based deposition methods, screen printing allows for straightforward fabrication under ambient conditions while also enabling control over film morphology.[37] A related area of interest concerns the influence of film texturing. Textured films have been shown to have improved luminescent properties. For example, highly textured Zn_2SiO_4:Mn^{2+} phosphor films exhibited a photoluminescence brightness of 65% relative to a commercially available Zn_2SiO_4:Mn^{2+} phosphor powder.[38]

This study presents a novel strategy for the synthesis of textured Zn_2SiO_4 films using screen printing assisted by a molten salt flux. By optimizing the ink formulation and using a single-crystal SiO_2 substrate, the highly textured Zn_2SiO_4 films with a pronounced preferential orientation along the (300) plane were fabricated. These films exhibited an intrinsic deep UV emission attributed to excitonic processes within the host lattice. Additionally, a green emission band was observed, likely originating from trace Mn^{2+} impurity. To the best of our knowledge, this study is the first to report deep UV emission from screen-printed Zn_2SiO_4 films, offering a rare-earth- and heavy metal-free solution for next-generation UV devices with a simple, scalable, and efficient fabrication process.

2. Experimental section

2.1. Film preparation

A series of inks was formulated with varying ZnO/SiO_2 ratios (0.5Zn, 1.0Zn, 1.5Zn, and 2.0Zn relative to the nominal 2.0ZnO : 1.0SiO_2 stoichiometry), each incorporating an eutectic mixture of 0.5NaCl–0.5KCl in a consistent 3 : 1 ratio relative to ZnO. The inks were prepared by mixing ZnO (symrise GmbH) with the eutectic salt mixture and an organic vehicle. The composition of the organic vehicle has been described in detail elsewhere.[37] The mixture was homogenized in a planetary ball mill (model YKM-1) using yttria-stabilized zirconia (YSZ) balls in 250 ml zirconia jars at 250 rpm for 8 h. To ensure optimal consistency, the ink was further processed in a three-roll mill (Dermamill 100SP Ointment Mill) with a 10 μm gap and a rotation speed of 25 rpm. This process was repeated three times to achieve a homogeneous ink.

The prepared ink was screen-printed onto single-side polished single-crystal quartz substrates (SiO_2 (0001), Biotain Crystal Co.) using a JM322R screen-printing device (Zhuhai Kaivo Optoelectronic Technology Co., Ltd). After deposition, a multi-step drying procedure was employed to remove the organic vehicle. The samples were heated at a controlled rate of 0.5 °C min^{-1} across temperatures of 150, 195, 270, 386, and 425 °C. Final thermal treatments were conducted at 1100 and 1200 °C in air for 4 h to ensure complete removal of the eutectic salt mixture, with heating and cooling rates of 5 °C min^{-1}.

2.2. Characterization

The phase composition of the synthesized Zn_2SiO_4 films was investigated using X-ray diffraction (XRD) on a Rigaku SmartLab SE diffractometer equipped with a D/teX Ultra 250 1D detector. Measurements were performed in a Bragg–Brentano configuration with Cu Kα radiation, scanning a 2θ range of 10–80°. The degree of preferred orientation in the films was quantified using the Lotgering factor (LF) calculated as follows:[39]

$$\mathrm{LF} = \frac{P - P_0}{1 - P_0}, \quad P = \frac{\sum I_{(00l)}}{\sum I_{(hkl)}}, \; P_0 = \frac{\sum I_{0(00l)}}{\sum I_{0(hkl)}} \qquad (1)$$

Here, I and I_0 represent the intensities of the diffraction peaks for the textured and randomly oriented samples, respectively. LF ranges from 0 to 1, where 0 indicates a random orientation and 1 corresponds to perfect alignment along the preferred growth direction.

The average crystallite size (D) was calculated using the Scherrer's formula:[40]

$$D = \frac{k\lambda}{\beta \cos\theta} \qquad (2)$$

where, k is a form factor (0.9), λ is the wavelength of the Cu kα radiation (1.54060 Å), β is peak broadening after instrumental correction (in radians), and θ is the Bragg diffraction angle.

The surface morphology and microstructure of the films were examined using field-emission scanning electron microscopy (FE-SEM, Zeiss ULTRA-55) equipped with energy dispersive X ray spectroscopy (EDS, Bruker Esprit 1.82 system) for elemental analysis.

Confocal Raman microscopy was performed using a WITEC Alpha 300R system equipped with a 532 nm excitation laser and a 100× objective lens (NA = 0.9) at an incident laser power of 0.5 mW. The optical diffraction resolution of the system was approximately 200 nm laterally and 500 nm vertically, with a spectral resolution of 0.02 cm^{-1}. Samples were mounted on a

piezo-driven scan platform, enabling precise positioning with 4 nm lateral and 0.5 μm vertical accuracy. Raman spectra were collected and processed using Witec Control Plus software to identify phase transformations and chemical interactions at the film–substrate interface.

The luminescent properties of Zn_2SiO_4 films were investigated using X-ray excited optical luminescence (XEOL), cathodoluminescence (CL), and synchrotron radiation-excited photoluminescence. XEOL measurements were conducted using an Edinburgh Instruments FLS980 spectrometer equipped with a Hamamatsu R298P photomultiplier and an X-ray tube (Oxford Instruments Neptune 5200) operating at 10–50 kV. CL analysis was performed using an electron beam with an energy of 10 keV, and low-temperature measurements were performed using an ARS close-cycle cryostat. Additional experimental details have been provided elsewhere.[41] Synchrotron radiation experiments were conducted at the FinEstBeAMS beamline, MAX IV Laboratory, Sweden, in the energy range of 4.5–11 eV.[42,43] To minimize higher-order incident light effects, MgF_2 or fused silica filters were employed depending on the excitation range. Luminescence was detected using an Andor Shamrock SR-303i spectrometer coupled with a Hamamatsu H8259-01 photon counting head. The excitation spectra were normalized to the incident photon flux using a calibrated AXUV100G photodiode. Luminescence spectra were converted into the energy scale upon using the Jacobian transformation procedure.

3. Results and discussion

3.1. Structural and morphological analysis

The fabrication of Zn_2SiO_4 films was studied as a function of ZnO/SiO_2 ratio (0.5Zn, 1.0Zn, 1.5Zn, and 2.0Zn) and thermal treatment (1100 °C and 1200 °C). This approach was designed to elucidate the fundamental mechanisms governing phase formation, crystallographic orientation, and microstructural evolution in the presence of the NaCl–KCl eutectic flux.

3.1.1. Phase formation and crystallographic texture. XRD analysis (Fig. 1a–d and 2a–d) revealed Zn_2SiO_4 as the predominant phase across all compositions, crystallizing in the rhombohedral structure (space group $R\bar{3}$, JCPDS card No. 37-1485, unit cell parameters: $a = b = 13.938$ Å, $c = 9.310$ Å).[44] Minor residual ZnO was detected only in the zinc-rich formulations, evidenced by a low-intensity diffraction peak at approximately 36.11°, corresponding to the (101) reflection of ZnO. However, the contribution of this secondary phase was minimal and nearly negligible. No systematic increase in ZnO-related reflections was observed upon increasing the thermal treatment from 1100 °C to 1200 °C, indicating preservation of the Zn_2SiO_4 phase within the investigated temperature range. This observation is further supported by uniform Zn, Si, and O distributions revealed by EDS (see SI, Fig. S1), confirming the overall phase purity of the films at both processing temperatures. The high phase conversion efficiency, particularly notable at sub-stoichiometric zinc contents, demonstrates the eutectic salt mixture's effectiveness in mediating the $ZnO–SiO_2$ reaction.

This conversion efficiency enhancement can be attributed to the two primary mechanisms: (i) increased atomic mobility in the molten state, and (ii) reduced interfacial energy barriers between reactant phases, as evidenced by the previous studies on similar systems.[45,46]

The films exhibited strong preferential orientation along the (300) crystallographic plane ($2\theta = 22.03°$), quantified using the Lotgering factor. At 1100 °C (Fig. 1e), LF values showed a distinct composition dependence: 0.47, 0.94, 0.83, and 0.29 for the 0.5Zn, 1.0Zn, 1.5Zn, and 2.0Zn compositions, respectively.

The near-unity LF value obtained for the 1.0Zn sample (LF = 0.94) indicates highly textured growth and suggests a favourable crystallographic alignment between the Zn_2SiO_4 (300) plane and the quartz (0001) substrate surface.

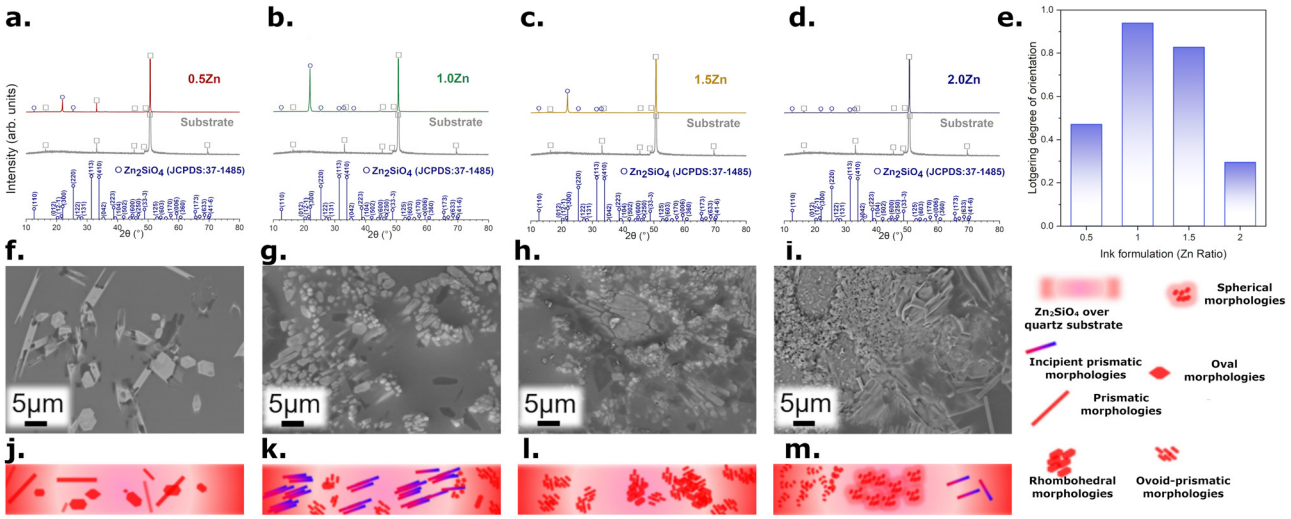

Fig. 1 Structural and morphological characterization of Zn_2SiO_4 films synthesized at 1100 °C: (a)–(d) XRD data for different ZnO concentrations (0.5Zn, 1.0Zn, 1.5Zn, and 2.0Zn), (e) calculated Lotgering factors, (f)–(i) SEM micrographs, and (j)–(m) schematic representations of observed morphologies. The legend indicates the different morphological features observed across compositions.

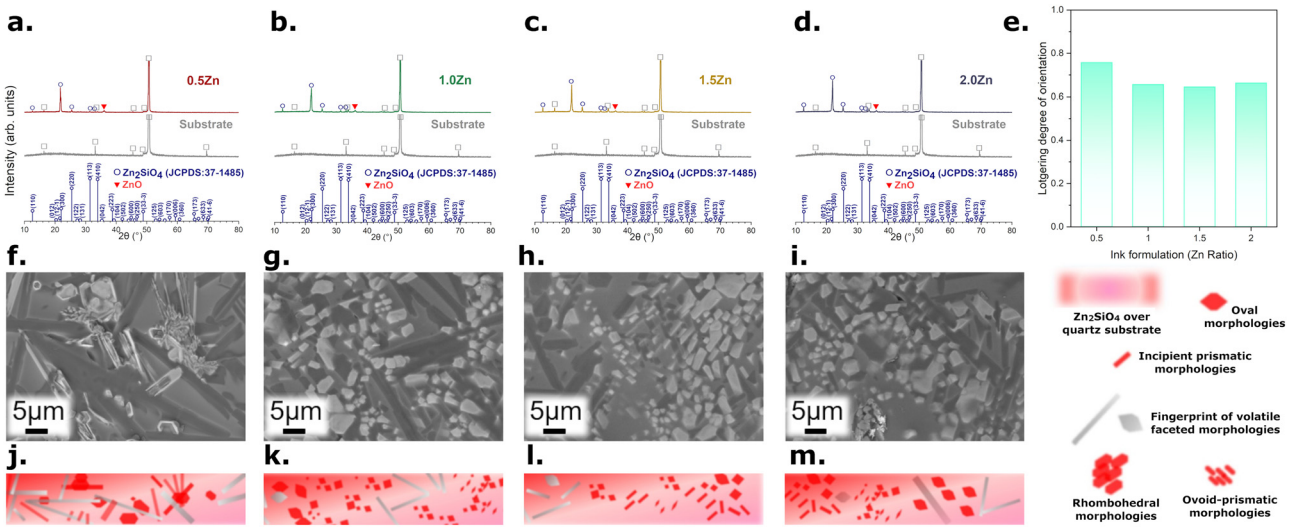

Fig. 2 Structural and morphological characterization of Zn_2SiO_4 films synthesized at 1200 °C: (a)–(d) XRD data for different ZnO concentrations (0.5Zn, 1.0Zn, 1.5Zn, and 2.0Zn), (e) calculated Lotgering factors, (f)–(i) SEM micrographs, and (j)–(m) schematic representations of observed morphologies. The legend indicates the different morphological features observed across compositions.

Quantitative lattice matching analysis (see SI, S2) indicates a low lattice mismatch (~−0.55%), suggesting good structural compatibility at the film–substrate interface. This structural compatibility, further promoted by the molten salt flux, enhances interfacial diffusion and favours oriented Zn_2SiO_4 nucleation during film growth.

The marked decrease in the Lotgering factor (LF) to 0.29 for the 2.0Zn sample indicates a significant disruption in the preferential crystallization process caused by excess ZnO. This disruption is likely driven by two concurrent mechanisms: (i) the formation of zinc-rich regions that exceed the local solubility limit in the flux, promoting uncontrolled nucleation, and (ii) increased competition between heterogeneous nucleation at the substrate interface and homogeneous nucleation within the film volume. These competing processes are consistent with classical nucleation theory, wherein local supersaturation can dominate over preferred orientation mechanisms.[47]

Thermal treatment at 1200 °C reduced this compositional sensitivity (Fig. 2e), yielding more uniform LF values (0.76, 0.66, 0.64, and 0.66 for 0.5Zn, 1.0Zn, 1.5Zn, and 2.0Zn, respectively). This convergence suggests a transition from kinetically controlled growth at 1100 °C to thermodynamically dominated processes at higher temperatures, where enhanced atomic mobility diminishes the influence of initial compositional variations.

To further quantify the microstructural characteristics of the films, the crystallite size was estimated from the broadening of the (300) diffraction peak. The calculated crystallite sizes for films synthesized at 1100 °C are approximately 69, 42, 40, and 35 nm for 0.5Zn, 1.0Zn, 1.5Zn, and 2.0Zn compositions, respectively. For the films processed at 1200 °C, the crystallite sizes increase to approximately 100, 62, 56, and 41 nm, indicating enhanced crystallite growth driven by higher atomic mobility at elevated temperature. The decrease in crystallite size with increasing Zn content at both temperatures suggests a higher nucleation density, which limits the growth of individual crystallites. This trend is consistent with the composition-dependent crystallization behaviour discussed above, where increased Zn content promotes competing nucleation processes. Overall, these results indicate that thermal treatment promotes crystallite growth, while compositional variations govern nucleation-controlled microstructural evolution.

3.1.2. Morphological evolution and growth mechanisms. The evolution of film morphology demonstrated a strong correlation with both compositional variation and crystallographic texture, revealing distinct growth mechanisms at different processing conditions. The observed morphology of the sample treated at 1100 °C reflects composition-dependent nucleation and growth behaviour influenced by the molten salt environment.

In the 0.5Zn films (Fig. 1f and j), the sparse distribution of predominantly rhombohedral particles aligns with the moderate texturing (LF = 0.47). This morphology suggests growth dominated by equilibrium crystal faces, where the slow growth rate, limited by zinc availability, allows the formation of well-defined crystallographic facets. The 1.0Zn composition (Fig. 1g and k) showed increased particle density with well-defined prismatic structures, corresponding to the maximum crystallographic ordering (LF = 0.94). This morphology represents optimal flux-mediated growth conditions, where the balanced stoichiometry and controlled supersaturation promote oriented crystal growth through interface-mediated nucleation processes. The 1.5Zn films (Fig. 1h and l) exhibited a transition to ovoid-prismatic morphologies with retained rhombohedral features. The increased particle concentration and morphological diversity reflect the onset of competing growth mechanisms, consistent with the decreased texture quality (LF = 0.83). In 2.0Zn films (Fig. 1i and m), the highest particle density and

mixed morphologies correlate with minimal texturing (LF = 0.29). The emergence of spherical features alongside ovoid-prismatic particles indicates a transition from faceted to rough growth modes, characteristic of systems exceeding critical supersaturation levels.

At 1200 °C, distinct morphological transformations occurred through enhanced diffusion processes. The characteristic "fingerprint" features observed in 0.5Zn samples (Fig. 2f and j) suggest concurrent processes of phase transformation and surface reconstruction through partial volatilization of the flux components. These surface features likely represent traces of localized substrate transformation, where quartz undergoes structural modification through interaction with the molten salt flux. The progressive reduction in these morphological characteristics with increasing zinc content correlates with enhanced reaction kinetics and higher particle density, leading to more uniform film surface coverage.

These observations highlight the complex interplay between kinetic and thermodynamic factors governing film morphology. At 1100 °C, film growth is primarily governed by composition-dependent kinetics, giving rise to distinct morphological regimes that are highly sensitive to local supersaturation and nucleation dynamics. In contrast, at 1200 °C, enhanced atomic mobility and surface diffusion promote more uniform morphological characteristics, largely independent on initial composition. This understanding underscores the potential for precise control of film microstructure through deliberate tuning of processing temperature and compositional parameters, offering a robust framework for tailoring texture and morphology in flux-assisted film synthesis.

The correlation between structural and morphological characteristics demonstrates the critical role of the molten salt flux in mediating both atomic transport and crystal growth processes. While XRD and SEM analyses have provided comprehensive insights into crystallographic ordering and surface features, a complete understanding of the film formation mechanism requires investigation of interfacial phenomena. The following section examines these aspects through depth-resolved Raman spectroscopy, which reveals the role of the molten salt flux in mediating substrate transformation and phase formation at the film–substrate interface.

3.1.3. Interface evolution and phase transformation analysis. Depth-resolved Raman spectroscopy provided critical insights into interfacial phenomena and phase evolution, complementing the structural and morphological characterization. The depth-profile images (Fig. 3a–h) illustrate the distribution of phases across the film–substrate interface, where the colour contrast distinguishes between Zn_2SiO_4 (red), cristobalite (green), and quartz substrate (blue).

At 1100 °C, the interface evolution demonstrates complex interplay between salt-mediated phase transformation with the assistance of molten salt and direct Zn_2SiO_4 formation. In the 0.5Zn films (Fig. 3a), the analysis reveals non-continuous Zn_2SiO_4 formation at the interface, characterized by distinct regions of Zn_2SiO_4 alternated with exposed quartz substrate. This discontinuous interface structure results from limited zinc

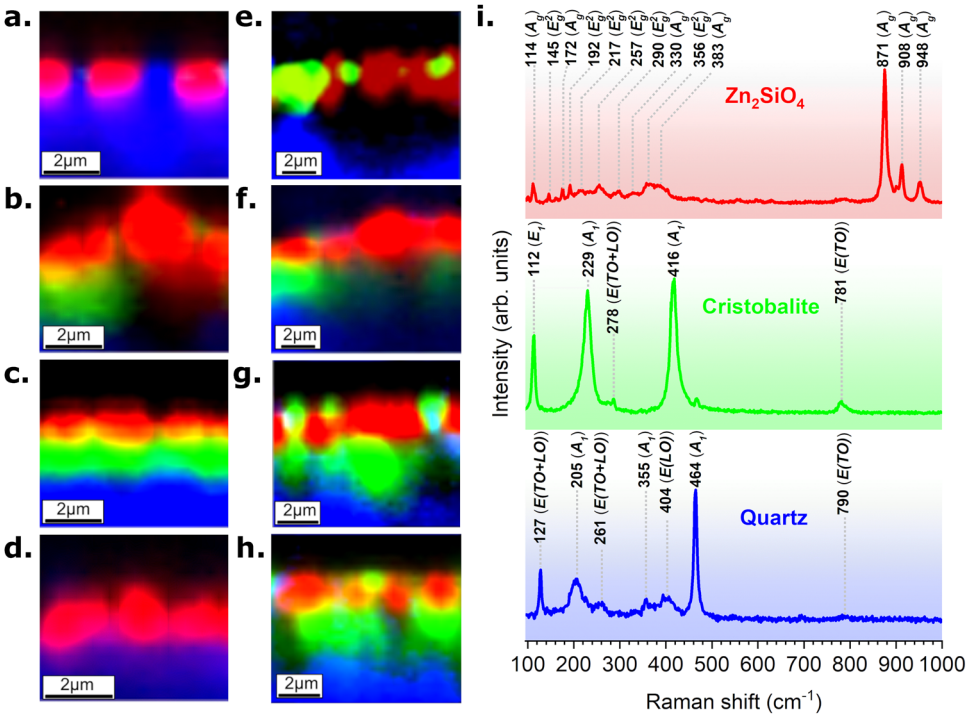

Fig. 3 Interface analysis of Zn_2SiO_4 films: (a)–(d) Raman depth profile images of films with different ZnO concentrations (0.5Zn, 1.0Zn, 1.5Zn, and 2.0Zn) synthesized at 1100 °C, (e)–(h) corresponding profiles at 1200 °C, and (i) representative Raman spectra showing characteristic vibrational modes of quartz, cristobalite, and Zn_2SiO_4 phases. Color contrast indicates quartz (blue), cristobalite (green), and Zn_2SiO_4 (red).

availability and insufficient concentration of Na^+ and K^+ ions from the eutectic salt mixture. These alkali metal ions, when present in adequate concentrations, can weaken Si–O bonds in the quartz structure through ionic interactions, facilitating the reorganization of the SiO_4 tetrahedra necessary for cristobalite formation.[48] The emergence of cristobalite in the 1.0Zn films (Fig. 3b) and its development into a continuous interlayer in the 1.5Zn samples (Fig. 3c) reflects the increasing effectiveness of the molten salt assisted transformation as more Na^+ and K^+ cations become available. This progression indicates that the eutectic salt mixture not only serves as a reaction medium but actively participates in the substrate transformation through cationic interactions with the quartz surface. The absence of cristobalite in the 2.0Zn films (Fig. 3d) reveals a competing mechanism where high zinc content creates sufficient chemical potential gradient to bypass the intermediate cristobalite formation. The direct formation of Zn_2SiO_4 is facilitated by enhanced ZnO dissolution in the molten flux, which promotes immediate reaction with the quartz substrate rather than enabling its phase transformation. This accelerated interface reaction correlates with the significantly reduced crystallographic texturing (Lotgering factor, LF = 0.29) observed in XRD analysis, indicating that rapid, uncontrolled nucleation at the interface disrupts the development of long-range orientational order. At 1200 °C (Fig. 3e–h), the consistent formation of cristobalite across all compositions indicates an enhancement in alkali ion diffusion and accelerated quartz transformation. This temperature-dependent behaviour appears largely independent of zinc content, suggesting that the dominant mechanism is thermally activated ionic mobility within the molten salt environment.[48] Supporting evidence from SEM analysis reveals characteristic surface features associated with high-temperature phase transitions, further corroborating the occurrence of quartz-to-cristobalite transformation. The interface structure results from competing kinetics between cristobalite formation and Zn_2SiO_4 growth, both assisted by the molten salt flux. The depth-resolved Raman analysis enabled precise measurement of film thicknesses across compositions and processing conditions. At 1100 °C, the thickness measurements (1.41 μm for 0.5Zn, 1.60 μm for 1.0Zn, 1.04 μm for 1.5Zn, and 1.40 μm for 2.0Zn) show maximum value at 1.0Zn, correlating with optimal crystallographic texturing (LF = 0.94) and initial cristobalite formation. These thickness measurements were further confirmed by cross-sectional SEM micrographs (see SI, Fig. S3). This correlation suggests that controlled interface transformation promotes uniform film growth through regulated mass transport. At 1200 °C, increased thicknesses (2.21, 1.71, 1.47, and 1.50 μm for 0.5Zn, 1.0Zn, 1.5Zn, and 2.0Zn, respectively) reflect enhanced diffusion processes, consistent with the more uniform morphological characteristics and LF values observed at higher temperatures.

The Raman spectra (Fig. 3i) provide detailed vibrational characteristics of the three distinct phases present in the system. The complete list of Raman modes and their assignments for all observed phases are presented in Table 1.

The quartz substrate exhibits characteristic modes at 127, 205, 261, 355, 404, 464, and 790 cm^{-1}, corresponding to the E(TO + LO), A_1, E(TO + LO), A_1, E(LO), A_1, and E(TO) symmetries, respectively.[40] The formation of cristobalite is confirmed by the distinctive peaks at 112 (E_1), 229 (A_1), 278 (E(TO + LO)), 416 (A_1), and 781 cm^{-1} (E(TO)),[50] reflecting the modified tetrahedral arrangement in the transformed phase. The Zn_2SiO_4 phase exhibits multiple vibrational modes between 114 and 948 cm^{-1}, with particularly intense bands at 871 cm^{-1} (symmetric Si–O stretching) and 908, 948 cm^{-1} (asymmetric stretching).[52]

The correlation between the interface structure and processing parameters reveals that the film formation mechanism is governed by the interplay between salt-mediated phase transformation and direct Zn_2SiO_4 crystallization controlled by alkali ion concentration, ZnO content, and processing temperature. Understanding these relationships enables precise control over interface structure and film thickness, demonstrating the effectiveness of the molten salt-assisted screen printing strategy for tunable thin film fabrication. The achievement of highly textured Zn_2SiO_4 films with well-defined interfaces and controlled thickness represents a crucial step in materials development for deep UV emission. The following section examines how

Table 1 Raman active modes and symmetry assignments of identified phases

SiO_2 (quartz)		SiO_2 (cristobalite)		Zn_2SiO_4	
Wavenumber (cm^{-1})	Assignment[49]	Wavenumber (cm^{-1})	Assignment[50]	Wavenumber (cm^{-1})	Assignment[51]
127	E(TO + LO)	112	E_1	114	A_g
205	A_1	229	A_1	145	E_g^2
261	E(TO + LO)	278	E(TO + LO)	172	A_g
355	A_1	416	A_1	192	E_g^2
404	E(TO)	781	E(TO)	217	E_g^2
464	A_1	—	—	257	E_g^2
790	E(TO)	—	—	290	E_g^2
—	—	—	—	330	A_g
—	—	—	—	356	E_g^2
—	—	—	—	383	A_g
—	—	—	—	871	A_g
—	—	—	—	908	A_g
—	—	—	—	948	A_g

these structural characteristics influence the deep UV luminescence properties, particularly focusing on the relationship between interface quality, crystallographic ordering, and emission in the deep UV spectral range.

3.2. Luminescence characterization

The luminescent properties of Zn_2SiO_4 films were investigated through three complementary spectroscopic techniques. X-ray excited optical luminescence at room temperature (RT) provided initial insights into the overall emission characteristics, while temperature-dependent cathodoluminescence measurements at RT and 6 K enabled detailed examination of the deep UV emission features. Further understanding of the excitation and emission processes was achieved through synchrotron radiation-excited photoluminescence at 6 K, which allowed selective excitation across a wide energy range and precise monitoring of the deep UV response.

3.2.1. X-ray luminescence. XEOL spectroscopy, effective for probing both surface and bulk luminescent properties,[53] has demonstrated significant utility in investigating silicate-based nanoscintillators.[54] Due to X-ray penetration depths significantly exceeding the film thicknesses (1.04–2.21 μm), the measurements probe contributions from both the films and the substrate. Fig. 4 presents RT XEOL spectra of all film compositions at both processing temperatures alongside the quartz substrate for comparison. The measurements reveal multiple emission features that reflect the complex interplay between composition, interface structure, and phase transformation processes established through our structural analyses. The dominant emission band centred at 2.38 eV (521 nm), characteristic of Mn^{2+} transitions in tetrahedral coordination,[55] exhibits maximum intensity in 1.5Zn samples at both processing temperatures. This band is absent in the substrate spectrum, confirming its origin from the film. The dominance of Mn^{2+} emission despite trace impurity levels indicates efficient energy transfer to these luminescent centres, enhancing the multifunctionality of the films in accordance with previous studies of silicate-based materials.[56] The high-energy region of the spectra, highlighted in the insets of Fig. 4a and b, provides insights into the relationship between structural evolution and luminescent properties. The band at 3.20 eV (387 nm), attributed to near-band-edge transitions in ZnO,[57] reflects residual ZnO identified in XRD analysis. The feature at 3.67 eV (338 nm), corresponding to non-bridging oxygen hole centres in silica,[58] appears in both film and substrate spectra, indicating contributions from the quartz substrate and SiO_2 polymorphs within the films.

A weak deep UV emission at 4.43 eV (280 nm), absent in the substrate, is also detected, showing the highest intensity in 1.5Zn samples at both synthesis temperatures. This composition-dependent behaviour is consistent with the interface development observed in 1.5Zn films, where the formation of a continuous cristobalite interlayer could potentially influence the emission properties.

To further investigate the nature of these emission features, particularly the deep UV response, temperature-dependent cathodoluminescence measurements were performed on the 1.5Zn films synthesized at both temperatures, which exhibited the most pronounced XEOL emission bands.

3.2.2. Cathodoluminescence. The cathodoluminescence spectra presented in Fig. 5 reveal significant temperature dependent emission characteristics in 1.5Zn films at RT *vs.* 6 K. RT spectra shown in Fig. 5a display the characteristic Mn^{2+} emission at 2.38 eV (521 nm) alongside a broad UV band with features at 3.73 eV (332 nm) and 4.13 eV (300 nm). Films synthesized at 1100 °C, characterized by higher crystallographic ordering (LF = 0.83), exhibit enhanced UV emission compared to those processed at 1200 °C (LF = 0.64).

The emission spectrum of the material recorded at low temperatures (6 K) is remarkably different from that measured at RT, as illustrated in Fig. 5b.

The deep UV emission shifts to higher energy (4.28 eV (290 nm)) and becomes dominant, while the Mn^{2+}-related green

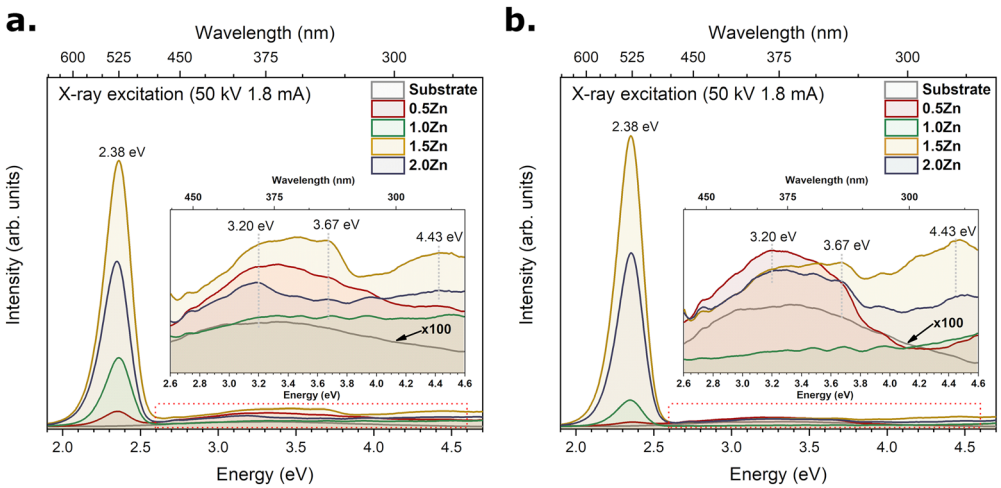

Fig. 4 X-ray excited luminescence analysis of Zn_2SiO_4 film–substrate systems: room temperature XEOL spectra of samples heat-treated at (a) 1100 °C and (b) 1200 °C with different ZnO concentrations (0.5Zn, 1.0Zn, 1.5Zn, and 2.0Zn). The quartz substrate spectrum is multiplied by 100 for better visualization. The insets highlight the high-energy region showing weak emission features in the UV range.

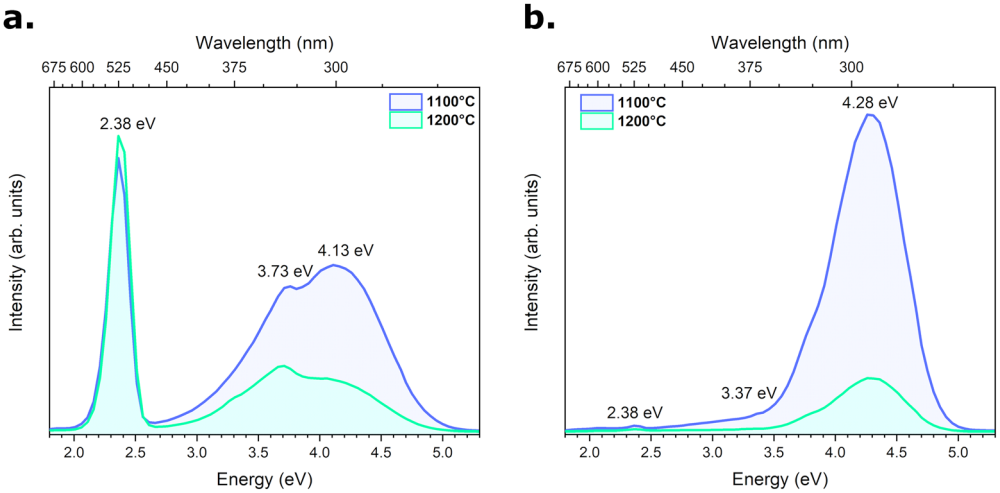

Fig. 5 Cathodoluminescence spectra of Zn_2SiO_4 films with 1.5Zn concentration synthesized at 1100 °C and 1200 °C, recorded at (a) room temperature and (b) 6 K.

emission is substantially suppressed. The film synthesized at 1100 °C shows markedly enhanced UV emission intensity relative to the sample synthesized at 1200 °C, which correlates with its improved crystallographic texturing and more homogeneous interface structure associated with the presence of a cristobalite interlayer.

The cristobalite interlayer is likely to provide a more structurally uniform transition region at the film–substrate interface, which may reduce the density of interfacial defects acting as non-radiative recombination centres. As a result, excitonic recombination within the Zn_2SiO_4 lattice is less hindered, contributing to the enhanced deep UV emission. In contrast, the more complex interface structure and increased lattice disorder in the 1200 °C sample are expected to introduce additional non-radiative recombination pathways for charge carriers, which compete with the radiative UV transitions.

The dependence of the CL spectrum on film quality suggests that the observed deep UV emission is predominantly intrinsic, arising from electronic transitions within the Zn_2SiO_4 crystal structure rather than from defect-related centres.

To further elucidate the nature of these transitions, synchrotron radiation based selective spectroscopy was employed, providing valuable information on the excitation mechanisms and the origin of electronic states responsible for the deep UV emission in Zn_2SiO_4.

3.2.3. Photoluminescence under synchrotron radiation excitation. To further investigate the mechanism responsible for the deep UV emission, synchrotron radiation studies were conducted at 6 K (Fig. 6).

As shown in Fig. 6a and b, the 2D excitation–emission maps reveal the luminescence response across a wide range of excitation energies. While samples synthesized at both temperatures exhibit similar spectral features, the sample synthesized at 1100 °C demonstrates notably higher emission intensity. The emission spectra presented in Fig. 6c, measured under 6 eV (207 nm) excitation, display a dominant peak at 4.43 eV (280 nm). This deep UV emission shows enhanced intensity in the sample synthesized at 1100 °C, corroborating the pattern observed in low-temperature CL measurements. At 6 K, both Mn^{2+} emission at 2.38 eV (521 nm) and the feature at 3.12 eV (397 nm) are significantly reduced.

Fig. 6d shows the excitation spectra monitored at 4.43 eV (280 nm), providing crucial insights into the origin of this deep UV emission. A recent study of sol–gel synthesized Zn_2SiO_4 powders demonstrated that this emission originates from host excitons, either self-trapped or perturbed by lattice defects such as oxygen vacancies.[28] The excitation spectra support and expand this understanding, showing an onset at 6.0 eV (207 nm), corresponding to the fundamental band gap of zinc silicate derived from partial density of states (PDOS) calculations[59] and consistent with the band gap values previously estimated from diffuse reflectance spectra of Zn_2SiO_4 powders synthesized at 1000, 1100, 1200, and 1300 °C[28] (see SI, Fig. S4). This excitation feature is therefore associated with band-to-band transitions leading to the formation of host excitons. In contrast, at higher excitation energies (above ~7 eV), the excitation processes increasingly involve transitions within the $[SiO_4]^{4-}$ units and defect-related states, as reported in previous studies.[60]

The high-energy region of the excitation spectra is thus related to the fundamental absorption processes characterized by the creation of mobile electrons in the conduction band and holes in the valence band due to the transitions from 2p O to 4s Zn and 3s Si states. These states have been shown to be well dispersive in Zn_2SiO_4 (see, *e.g.*, ref. 27), enabling high mobility of electrons in the conduction band, which in turn can lead to high energy losses of electrons with high kinetic energy at the crystal surface and defects.[61] This renders luminescence highly sensitive to material structural quality and defect distribution. Indeed, in the sample synthesized at 1100 °C, this high-energy region of the excitation spectrum is remarkably intense, indicating differences in the excitation processes and carrier relaxation dynamics between the two samples.

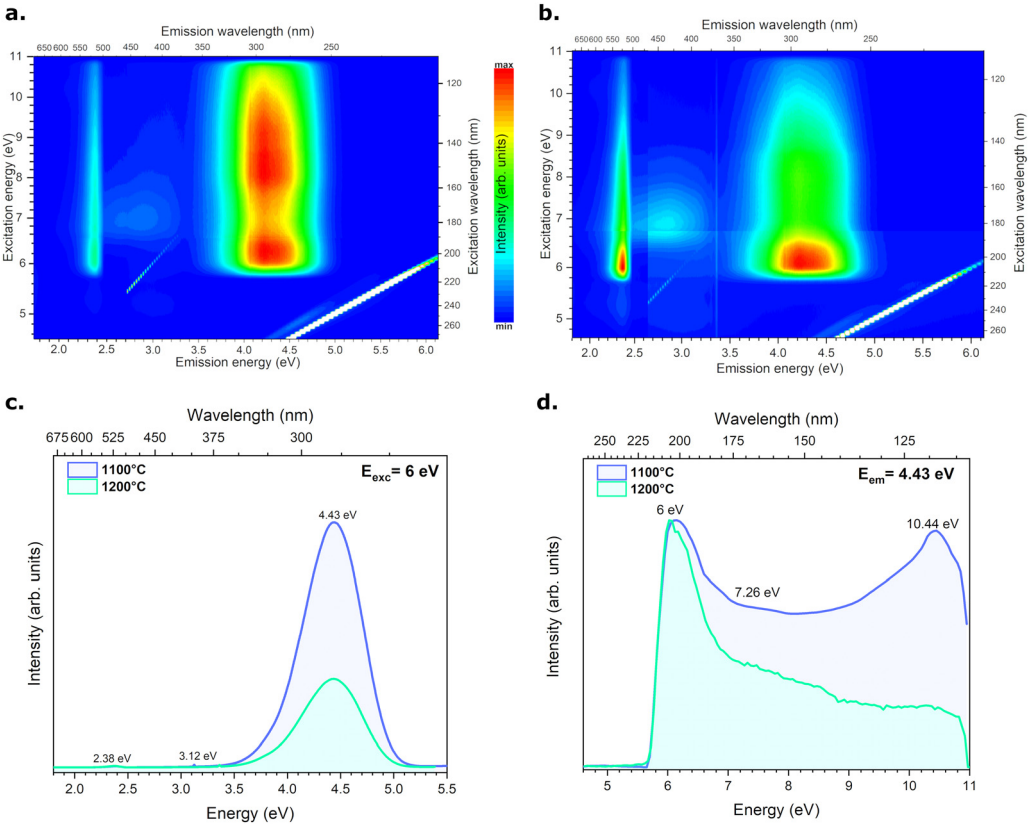

Fig. 6 Synchrotron excitation analysis of Zn_2SiO_4 films with 1.5Zn concentration: (a) and (b) 2D excitation–emission maps of films synthesized at 1100 °C (a) and 1200 °C (b) and (c) emission spectra under 6 eV excitation, and (d) excitation spectra monitored at 4.43 eV emission. All measurements were performed at 6 K.

The influence of lattice defects can be considered in terms of intrinsic point defects and structural disorder. In related oxide systems such as $ZnAl_2O_4$, deep UV emission has been linked to excitons perturbed by oxygen vacancies, as confirmed by electron paramagnetic resonance (EPR) studies.[21] Similar defect-exciton interactions may also be expected in Zn_2SiO_4, where lattice imperfections can influence exciton localization and recombination. However, the specific nature and concentration of defects in the present films cannot be determined within the scope of this study. Further investigations, such as time-resolved photoluminescence and EPR measurements, will be pursued to clarify the role of defects in the luminescence response of Zn_2SiO_4.

The stronger deep UV emission in the sample synthesized at 1100 °C is consistent with its well-defined cristobalite interlayer and high crystallographic texturing (LF = 0.83), which may contribute to reduced non-radiative recombination. Importantly, the lower emission intensity observed in the 1200 °C sample is unlikely to originate from thermal decomposition of Zn_2SiO_4. The ZnO–SiO_2 phase diagram indicates that Zn_2SiO_4 remains thermodynamically stable up to approximately 1400 °C,[62,63] and our previous quantitative phase analysis of powders synthesized up to 1300 °C confirmed phase stability under comparable conditions.[28,29] Thermogravimetric and differential scanning calorimetry (TGA–DTG–DSC) of Zn_2SiO_4 powders synthesized at 1300 °C *via* the molten salt route demonstrate that fully crystallized Zn_2SiO_4 remains thermally stable upon reheating within the investigated temperature range (see SI, Fig. S5). Therefore, the observed luminescence differences are attributed to microstructural and interfacial variations rather than changes in phase composition.

4. Conclusions

Zn_2SiO_4 has been identified as a promising rare-earth-free deep UV emitter. However, the extension of its intrinsic emission properties to film form remains limited. The successful fabrication of highly textured Zn_2SiO_4 films featuring well-defined interfaces and controlled thickness in this work demonstrates the feasibility of intrinsic deep UV emission in film form. The optimal structural and luminescent properties were achieved in samples synthesized at 1100 °C with a 1.5Zn composition, where the formation of a continuous cristobalite interlayer and a high Lotgering factor (LF = 0.83) enabled superior crystallographic texturing.

This study addresses the relationship between processing-induced structural evolution, interface formation, and intrinsic deep UV emission in Zn_2SiO_4 films.

By systematically correlating processing conditions with structural evolution and optical response, this work clarifies

how interfacial phase transformation and crystallographic orientation influence intrinsic deep UV emission in Zn_2SiO_4 films.

The molten salt flux plays a multifaceted role by mediating phase formation, controlling interface evolution, and promoting oriented growth, although excessive ZnO disrupts texture development. Spectroscopic and synchrotron-based studies indicate that the deep UV emission at 4.43 eV (280 nm) arises from intrinsic electronic transitions involving self-trapped or defect-perturbed excitons in Zn_2SiO_4. The strong correlation between structural order and emission intensity highlights the critical impact of controlled processing on optical performance.

The screen printing method assisted by a molten salt eutectic flux provides a simple, scalable, and effective route for synthesizing phase-pure, highly oriented Zn_2SiO_4 films without complex vacuum processing.

Overall, this work addresses the limited understanding of intrinsic deep UV emission in Zn_2SiO_4 films and demonstrates the potential of rare-earth- and heavy-metal-free Zn_2SiO_4 materials for next-generation deep-UV radiation sources, while the structural control achieved here illustrates the broader potential of this processing approach for oxide-based photonic materials.

Author contributions

Jallouli Necib: writing – review & editing, writing – original draft, validation, methodology, investigation, formal analysis, conceptualization. Eduard Feldbach: writing – review & editing, formal analysis. Ivo Romet: writing – review & editing, investigation. Vitali Nagirnyi: writing – review & editing, writing – original draft, validation, methodology, investigation. Irina Hussainova: writing – review & editing, validation, investigation. Thomas Jüstel: writing – review & editing, investigation. Rocío E. Rojas-Hernandez: writing – review & editing, writing – original draft, visualization, validation, supervision, software, resources, project administration, methodology, investigation, funding acquisition, formal analysis, data curation, conceptualization.

Conflicts of interest

The authors declare no conflict of interest.

Data availability

Data for this article, including raw XRD patterns, SEM images, cathodoluminescence spectra, and X-ray excited optical luminescence spectra, are available at the TalTech Data Repository at https://doi.org/10.48726/qgpvy-k5q16. Supplementary information: containing additional cross-sectional SEM micrographs demonstrating film thickness and interface morphology across different processing temperatures and compositions. See DOI: https://doi.org/10.1039/d6tc00560h.

Acknowledgements

The financial support from the Estonian Research Council through grants PSG466 (R. E. Rojas-Hernandez), PRG643 and PRG3028 (I. Hussainova), and PRG2733 (V. Nagirnyi) is gratefully acknowledged. Researchers from the University of Tartu, Estonia were supported also by the ERDF funding in Estonia granted to the Centre of Excellence TK141 "Advanced materials and high-technology devices for sustainable energetics, sensorics and nanoelectronics (HiTechDevices)" (grant no. TK141 2014–2020.4.01.15-0011). R. E. R. H. acknowledges the financial support from project PID2023-153398OB-I00 funded by MCIU/AEI/10.13039/501100011033 and the European Social Fund Plus (ESF+). We acknowledge MAX IV Laboratory for beamtime on the FinEstBeAMS beamline under Proposal 20230209. Research conducted at MAX IV, a Swedish national user facility, is supported by the Swedish Research council under contract 2018-07152, the Swedish Governmental Agency for Innovation Systems under contract 2018-04969, and Formas under contract 2019-02496.

References

1 A. Gidari, S. Sabbatini, S. Bastianelli, S. Pierucci, C. Busti, D. Bartolini, A. M. Stabile, C. Monari, F. Galli, M. Rende, G. Cruciani and D. Francisci, *Viruses*, 2021, **13**, 408.
2 M. Kösea, Ç. K. Akkanb, H. Karabacakc and A. Kolumand, *J. Biomed. Res. Environ. Sci.*, 2024, **5**, 1358–1370.
3 S. Wang, Z. Wu, L. Sun, J. Ren, X. Zheng, J. Zhang and J. Ren, *J. Mater. Chem. C*, 2025, **13**, 6302–6308.
4 T. Tanaka, N. Sasaki, A. Krisnanda, M. Shinohara, H. Z. Amin, S. Horibe, K. Ito, M. Iwaya, A. Fukunaga, K. I. Hirata and Y. Rikitake, *J. Am. Heart Assoc.*, 2024, **13**, e031639.
5 S. B. Maji, A. Vanetsev, V. Nagirnyi, K. Chernenko, E. Feldbach, J. Kozlova, H. Mändar, I. Romet, M. Rähn and M. Kirm, *J. Mater. Chem. C*, 2025, **13**, 10139–10151.
6 W. Liu, Y. Wang, H. Qiu, D. Chen, S. Wu, Q. Ji, B. Chang, Y. Li, H. Zhao, Y. Tan and Y. Gu, *Biomed. Opt. Express*, 2024, **15**, 4081–4100.
7 L. L. Barnkob, A. Argyraki, P. M. Petersen and J. Jakobsen, *Food Chem.*, 2016, **212**, 386–391.
8 R. Escobar-Bravo, P. G. Klinkhamer and K. A. Leiss, *Front. Plant Sci.*, 2017, **8**, 278.
9 R. Hidalgo-Sanz, M. Á. Del-Castillo-Alonso, S. Sanz, C. Olarte, J. Martínez-Abaigar and E. Núñez-Olivera, *Agriculture*, 2024, **14**, 681.
10 United Nations Environment Programme (UNEP), Minamata convention on mercury, United Nations Environment Programme, Nairobi, Kenya, 2013.
11 P. C. Ricci, *Crystals*, 2020, **10**, 559.
12 H. Diao, H. Yang, T. Tan, G. Ren, M. You, L. Wu, M. Yang, Y. Bai, S. Xia, S. Song and M. Quintana, *Miner. Eng.*, 2024, **216**, 108889.
13 S. Liu, T. Lu, Y. Yuan, J. Cao, W. Wan, T. Li, T. Wang, Z. Chen, X. Sun and X. Wang, *Adv. Funct. Mater.*, 2025, **35**, 2503580.

14 F. Feng, Y. Liu, K. Zhang, H. Yang, B. R. Hyun, K. Xu, H. S. Kwok and Z. Liu, *Nat. Photonics*, 2025, **19**, 101–108.
15 Z. Lv, Z. Liao, X. Liu, J. Jiang, H. Geng, S. Qi, S. Liu and S. Zhou, *Laser Photonics Rev.*, 2026, e01763.
16 D. X. Zhu, G. Wang and Y. F. Li, *Front. Phys.*, 2025, **13**, 1718751.
17 X. Xu, H. P. Liang, Q. S. Huang, Z. Liu, B. Q. Zhao, S. Y. Xu, C. N. Li, Z. K. Zhou, J. Li, S. H. Wei and X. Zhang, *J. Am. Chem. Soc.*, 2024, **146**, 12864–12876.
18 R. K. Guntu, S. S. Devi, P. Ashok, G. Bhikshamaiah, N. R. K. Chand, S. Sripadha, P. S. Prasad and C. S. Rao, *J. Mol. Liq.*, 2024, **404**, 124933.
19 R. K. Guntu, *J. Mol. Struct.*, 2022, **1248**, 131533.
20 R. E. Rojas-Hernandez, F. Rubio-Marcos, I. Romet, A. Del Campo, G. Gorni, I. Hussainova, J. F. Fernandez and V. Nagirnyi, *Inorg. Chem.*, 2022, **61**, 11886–11896.
21 R. E. Rojas-Hernandez, F. Rubio-Marcos, I. Romet, E. Feldbach, M. Buryi, D. John, R. Ivanov, I. Hussainova, J. F. Fernandez and V. Nagirnyi, *Appl. Mater. Today*, 2024, **38**, 102230.
22 S. Karmakar, I. H. Emu, M. A. Halim, P. K. Sarkar, M. Sultana, A. Tasnim, M. A. Hamid, I. F. Shiam, R. Droopad and A. Haque, *J. Appl. Phys.*, 2024, **135**, 042603.
23 R. Gerdes, D. Enseling, M. Haase and T. Jüstel, *J. Lumin.*, 2018, **198**, 410–417.
24 P. V. Ramakrishna, D. B. R. K. Murthy, D. L. Sastry and K. Samatha, *Spectrochim. Acta, Part A*, 2014, **129**, 274–279.
25 S. Tripathi, R. Bose, A. Roy, S. Nair and N. Ravishankar, *ACS Appl. Mater. Interfaces*, 2015, **7**, 26430–26436.
26 G. Essalah, G. Kadim, A. Jabar, R. Masrour, M. Ellouze, H. Guermazi and S. Guermazi, *Ceram. Int.*, 2020, **46**, 12656–12664.
27 S. Z. Karazhanov, P. Ravindran, H. Fjellvåg and B. G. Svensson, *J. Appl. Phys.*, 2009, **106**, 123701.
28 J. Necib, E. Feldbach, I. Romet, V. Nagirnyi, I. Hussainova and R. E. Rojas-Hernandez, *J. Lumin.*, 2025, **277**, 121070.
29 J. Necib, E. Feldbach, I. Romet, V. Nagirnyi, I. Hussainova, T. Jüstel and R. E. Rojas-Hernandez, *Ceram. Int.*, 2025, **51**, 34922–34931.
30 X. Feng, X. Yuan, T. Sekiguchi, W. Lin and J. Kang, *J. Phys. Chem. B*, 2005, **109**, 15786–15790.
31 C. Li, Y. Bando, B. Dierre, T. Sekiguchi, Y. Huang, J. Lin and D. Golberg, *Nanoscale Res. Lett.*, 2010, **5**, 773–780.
32 B. Dierre, X. Yuan and T. Sekiguchi, *Sci. Technol. Adv. Mater.*, 2010, **11**, 043001.
33 T. Furukawa, S. Kanamori, M. Fukuta, Y. Nawa, H. Kominami, Y. Nakanishi, A. Sugita, W. Inami and Y. Kawata, *Opt. Express*, 2015, **23**, 18630–18637.
34 K. C. Peng, H. C. Kao, S. J. Liu, K. L. Tsai and J. C. Lin, *Jpn. J. Appl. Phys.*, 2013, **52**, 11NB04.
35 H. P. Kuo, H. A. Tsai, A. N. Huang and W. C. Pan, *Appl. Energy*, 2016, **164**, 1003–1011.
36 W. Yao, Q. Tian, J. Liu, Z. Wu, S. Cui, J. Ding, Z. Dai and W. Wu, *J. Mater. Chem. C*, 2016, **4**, 6327–6335.
37 R. E. Rojas-Hernandez, F. Rubio-Marcos, A. Serrano, I. Hussainova and J. F. Fernandez, *J. Eur. Ceram. Soc.*, 2020, **40**, 1677–1683.
38 J. Park, K. Park, J. Lee, J. Kim, S. M. Kim and P. Kung, *Jpn. J. Appl. Phys.*, 2010, **49**, 042603.
39 F. K. Lotgering, *J. Inorg. Nucl. Chem.*, 1959, **9**, 113–123.
40 U. Holzwarth and N. Gibson, *Nat. Nanotechnol.*, 2011, **6**, 534.
41 E. Feldbach, E. Tõldsepp, M. Kirm, A. Lushchik, K. Mizohata and J. Räisänen, *Opt. Mater.*, 2016, **55**, 164–167.
42 V. Pankratov, R. Pärna, M. Kirm, V. Nagirnyi, E. Nõmmiste, S. Omelkov, S. Vielhauer, K. Chernenko, L. Reisberg, P. Turunen, A. Kivimäki, E. Kukk, M. Valden and M. Huttula, *Radiat. Meas.*, 2019, **121**, 91–98.
43 R. Pärna, R. Sankari, E. Kukk, E. Nõmmiste, M. Valden, M. Lastusaari, K. Kooser, K. Kokko, M. Hirsimäki, S. Urpelainen, P. Turunen, A. Kivimäki, V. Pankratov, L. Reisberg, F. Hennies, H. Tarawneh, R. Nyholm and M. Huttula, *Nucl. Instrum. Methods Phys. Res.*, 2017, **859**, 83–89.
44 M. Masjedi-Arani and M. Salavati-Niasari, *Ultrason. Sonochem.*, 2016, **29**, 226–235.
45 G. Hu, W. Li, G. He, J. Wang, Y. Zhao, Y. Zhang and B. Yao, *Ceram. Int.*, 2016, **42**, 7852–7856.
46 H. Chen, G. Wang, L. Zhao, X. He, C. Huang, W. Li, W. Fang and X. Du, *Microporous Mesoporous Mater.*, 2017, **243**, 331–338.
47 L. Li, A. Fijneman, J. Kaandorp, J. Aizenberg and W. Noorduin, *Proc. Natl. Acad. Sci. U. S. A.*, 2018, **115**, 3575.
48 W. Li, C. Xu, A. Xie, K. Chen, Y. Yang, L. Liu and S. Zhu, *Crystals*, 2021, **11**, 1481.
49 J. F. Scott and S. P. S. Porto, *Phys. Rev.*, 1967, **161**, 903–910.
50 J. Etchepare, M. Merian and P. Kaplan, *J. Chem. Phys.*, 1978, **68**, 1531–1537.
51 N. S. Bekturganov, M. R. Bissengaliyeva and D. B. Gogol, *Eurasian Chem.-Technol. J.*, 2013, **15**, 227.
52 M. Czaja, R. Lisiecki, R. Juroszek and T. Krzykawski, *Minerals*, 2021, **11**, 1215.
53 H. Ji, Z. Huang, Z. Xia, M. S. Molokeev, V. V. Atuchin, M. Fang and S. Huang, *Inorg. Chem.*, 2014, **53**, 5129–5135.
54 W. Sun, T. Shi, L. Luo, X. Chen, P. Lv, Y. Lv, Y. Zhuang, J. Zhu, G. Liu, X. Chen and H. Chen, *Adv. Mater.*, 2019, **31**, 1808024.
55 N. Rakov, F. Matias, Y. Xing and G. S. Maciel, *Opt. Mater.: X*, 2024, **24**, 100359.
56 X. Jiang, X. Gao, L. Li, P. Zhou, S. Wang, T. Liu, J. Zhou, H. Zhang, K. Huang, Y. Li and M. Wang, *ACS Appl. Mater. Interfaces*, 2023, **17**, 21228–21238.
57 C. Baratto, E. Comini, M. Ferroni, G. Faglia and G. Sberveglieri, *CrystEngComm*, 2013, **15**, 7981–7986.
58 H. He, Y. Wang and Y. Zou, *J. Phys. D: Appl. Phys.*, 2003, **36**, 2972.
59 H. J. Chang, H. D. Park, K. S. Sohn and J. D. Lee, *J. Korean Phys. Soc.*, 1999, **34**, 545–548.
60 V. S. Kortov, K. A. Sergeeva, V. A. Pustovarov and A. A. Rempel, *J. Surf. Invest.: X-Ray, Synchrotron Neutron Tech.*, 2017, **11**, 727–731.
61 D. Spassky, V. Mikhailin, M. Nazarov, M. N. Ahmad-Fauzi and A. Zhbanov, *J. Lumin.*, 2012, **132**, 2753–2762.
62 E. N. Bunting, *J. Am. Ceram. Soc.*, 1930, **13**, 5–10.
63 L. Xia, Z. Liu and P. A. Taskinen, *J. Eur. Ceram. Soc.*, 2015, **35**, 4005–4010.